Catalysis Science & Technology

PAPER

View Article Online
View Journal | View Issue

Cite this: *Catal. Sci. Technol.*, 2016, **6**, 6861

Understanding oxidative dehydrogenation of ethane on Co_3O_4 nanorods from density functional theory

Victor Fung,[a] Franklin (Feng) Tao[b] and De-en Jiang*[a]

Received 4th April 2016,
Accepted 20th May 2016

DOI: 10.1039/c6cy00749j

www.rsc.org/catalysis

Co_3O_4 is a metal oxide catalyst with weak, tunable M–O bonds promising for catalysis. Here, density functional theory (DFT) is used to study the oxidative dehydrogenation (ODH) of ethane on Co_3O_4 nanorods based on the preferred surface orientation (111) from the experimental electron-microscopy image. The pathway and energetics of the full catalytic cycle including the first and second C–H bond cleavages, hydroxyl clustering, water formation, and oxygen-site regeneration are determined. We find that both lattice O and Co may participate as active sites in the dehydrogenation, with the lattice-O pathway being favored. We identify the best ethane ODH pathway based on the overall energy profiles of several routes. We identify that water formation from the lattice oxygen has the highest energy barrier and is likely a rate-determining step. This work of the complete catalytic cycle of ethane ODH will allow further study into tuning the surface chemistry of Co_3O_4 nanorods for high selectivity of alkane ODH reactions.

1. Introduction

The conversion of alkanes such as ethane and propane into olefins is an industrially and economically important process and produces a significant portion of highly desired feedstock used in the chemical industry. Due to the high expense and energy cost of steam cracking to produce these olefins, there has been intense effort in recent years to search for more selective and energetically efficient methods.[1] Catalytic oxidative dehydrogenation (ODH) has been proposed as an attractive alternative with the advantage of being more thermodynamically favored and with the potential to have greater selectivity at lower temperatures. These qualities of the ODH pathway would significantly reduce the costs of olefin production to suit the quickly increasing global demand.[2]

A wide variety of catalytic materials have been studied for the ODH reaction: earth-abundant metal oxides[3–18] appear as cost-effective and more viable alternatives to noble metal catalysts. In particular, spinel cobalt oxide (Co_3O_4) is a particularly promising candidate which has been found to be very active in many oxidation reactions including those of CO,[19] CH_4,[20] and other hydrocarbons.[21] A major factor in the catalytic activity of Co_3O_4 is the very weak M–O bond among other transition metal oxides[22] and the presence of readily generated oxygen vacancies at the surface.[20,23] Experimental and theoretical studies have identified a number of stable surfaces on the Co_3O_4 nanoparticles and nanorods, including the (100), (110) and (111) surfaces.[19,21,24–32]

Of these surfaces, the high activity of the (110) facet for reactions such as CO oxidation has been widely reported; however, the (111) surface has been found to be readily formed[26,29] and more thermodynamically stable[28] than the (110) surface. Therefore, the morphology of Co_3O_4 nanocatalysts may greatly impact their catalytic activity due to the difference in preferred surface orientations and it would be very interesting to understand the change in the reaction mechanism on those different surfaces. DFT has been employed in many previous studies on the surface properties and catalytic activity of Co_3O_4 that is thought to proceed *via* the Mars–van Krevelen mechanism involving the lattice oxygen on the surface.[33–37] These active oxygen species react and desorb in products to form vacancies which must then be regenerated from gaseous molecular oxygen in order to maintain the catalytic activity of the surface.

Several recent works have shown that modifying the pure Co_3O_4 surface can improve its performance for alkane activation. These methods include doping transition metals such as Ni to facilitate the oxidation of alkanes[20] and depositing non-metallic elements such as Si and Ge onto the surface of Co_3O_4 nanorods to tune the selectivity of the catalyst towards the ethane ODH product.[38] However, the underlying mechanism of how the modification of the Co_3O_4 surface by other elements changes the activity and selectivity of the nanocatalyst for ethane ODH remains unclear.

[a] *Department of Chemistry, University of California, Riverside, CA 92521, USA. E-mail: de-en.jiang@ucr.edu; Tel: +1 951 827 4430*
[b] *Department of Chemical and Petroleum Engineering and Department of Chemistry, University of Kansas, Lawrence, KS 66045, USA*

As a first step toward understanding the roles of morphology control and surface modification in Co_3O_4 nanocatalysts for ethane ODH, herein we present the detailed analysis of the full catalytic cycle from first principles based on the experimental determination of the preferred surface orientation of Co_3O_4 nanorods. We elucidate the nature of the two C–H activations to produce ethylene, the formation of water, and the regeneration of the oxygen sites to complete the catalytic cycle. These insights will provide a better understanding of the role of the different active surface atoms on a specific surface orientation in determining the selectivity and yield of the ethane ODH pathway that may allow one to design better Co_3O_4 nanocatalysts.

2. Experimental and computational methods

Co_3O_4 nanorods were synthesized *via* a previously reported method.[23,39] Briefly, cobalt acetate tetrahydrate was dissolved in ethylene glycol and heated to 160 °C under N_2, then reacted with a slowly added $NaHCO_3$ aqueous solution under vigorous stirring. After centrifugation, a purple precipitate was obtained, which was then dried at 50 °C under vacuum and calcined at 350 °C in air to yield the Co_3O_4 nanorods. Their crystalline form was checked using powder X-ray diffraction. Then, the nanorods were imaged by high-angle annular dark field (HAADF) scanning transmission electron microscopy (STEM) on a JEOL JEM-ARM200F transmission electron microscope at 200 kV. Based on the surface orientation of the Co_3O_4 nanorods from the STEM images, we then employed density functional theory (DFT) to examine the ethane ODH pathways on it.

All DFT calculations were performed using the Vienna *ab initio* simulation package (VASP).[40,41] The on-site Coulomb interaction was included using the DFT+U method by Dudarev *et al.*[42] with a Hubbard parameter of U = 2 eV for Co, which yielded band gaps in good agreement with the experimental results and was used to good effect in previous DFT studies of Co_3O_4 surface chemistry and catalysis.[19,20] The Perdew–Burke–Ernzerhof (PBE)[43] form of the generalized-gradient approximation (GGA) was chosen for electron exchange and correlation. The electron–core interaction was described using the projector-augmented wave method (PAW).[44,45] A kinetic energy cutoff of 450 eV was used for the planewaves, and the Brillouin zone was sampled using a 3 × 3 × 1 Monkhorst–Pack scheme.[46] All calculations in this work were performed with spin polarization. The slab was created containing 11 layers with the bottom 9 layers frozen in their bulk positions. The optimized lattice constant was found to be 8.14 Å, in very good agreement with the experimental value of 8.09 Å.[47]

The adsorption energies were defined by $E_{ads} = E_{surface+adsorbate} - (E_{surface} + E_{adsorbate})$, where the energy of the adsorbate $E_{adsorbate}$ was computed by placing an adsorbate molecule in a cubic cell of 10 Å in side length (in other words, the molecule and its nearest periodic images are separated by about 10 Å vacuum). Transition states were found *via* a two-step approach, using both the nudged elastic band method (NEB) and the dimer method[48] implemented in the VASP-VTST package by Henkelman *et al.*[49] The initial and final states of the reactions were first identified and optimized, and were used to generate 8–10 equally spaced images between them through linear interpolation. These images were then minimized under the NEB constraints to forces of ~0.4–0.2 eV $Å^{-1}$ in order to generate an approximate minimum reaction energy path. The highest two energy images along the path were then used to generate a starting geometry for the dimer method, until reaching an energy convergence of 0.05 eV $Å^{-1}$. Selected transition states were confirmed by vibrational frequency analysis to verify the effectiveness of this method and the convergence criterion.

3. Results and discussion

3.1 Surface structure of Co_3O_4 nanorods

Recent work has shown that Si and Ge-modified Co_3O_4 nanorods improved the selectivity and yield of ethane ODH, but the molecular-level mechanism is still unclear.[38] Here, we first direct our attention to modeling the mechanism of ethane ODH on the experimentally produced Co_3O_4 nanorods, so we can examine the role of the surface modification in the future. The synthesized Co_3O_4 nanorods were imaged *via* scanning tunneling electron microscopy (STEM) (Fig. 1A and B). The atomic-resolution HAADF-STEM image (Fig. 1B) suggests that the Co_3O_4(111) surface is preferentially exposed in this sample of Co_3O_4 nanorods. This information about the surface orientation provides a desired foundation for our DFT modeling. The Co_3O_4(111) surface and the Co_3O_4(110) surface are both catalytically active and stable surfaces confirmed from both experimental and theoretical studies in the previous literature.[26,28,29] Based on the STEM images, we chose the (111) surface as a model active surface in this work.

The Co_3O_4(111) surface can be terminated into six inequivalent layers; we chose the one with the lowest surface energy based on previous DFT calculations.[28] This surface model terminates to yield tetrahedral Co^{2+} atoms and triply coordinated oxygen atoms on the surface (Fig. 1C). The surface lattice oxygens can be categorized into two types: O^A, which are triply coordinated to the subsurface cobalt (Co^{3+}); O^B, which are doubly coordinated to the subsurface Co but also singly coordinated to the surface Co (Fig. 1C). After relaxation of this Co_3O_4(111) surface termination, the surface Co–O^B bonds shorten from 1.952 to 1.788 Å. The O^A–Co bonds shorten from 1.932 to 1.885 Å. In predicting the reactivity of the two inequivalent lattice O atoms, we find that O^A has a lower vacancy formation energy of 2.488 eV and a higher average Bader charge of −0.767 |e|. Meanwhile, O^B has a vacancy formation energy of 2.946 eV and an average Bader charge of −0.860 |e|. The average Bader charge of the surface Co was found to be 1.298 |e|. The lower O^A vacancy formation energy suggests that the O^A oxygen is more active and more likely to react to result in a vacancy.

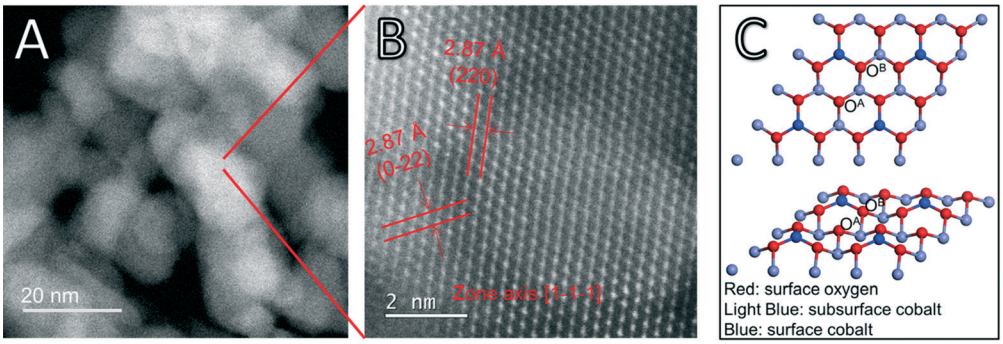

Fig. 1 (A) STEM image of a large area of a Co_3O_4 nanorod sample. (B) HAADF-STEM image of a small area of the Co_3O_4 nanorod sample, marked with lattice fringes. (C) The surface model used in this DFT study for the same $Co_3O_4(111)$ surface: only the first three layers are shown for clarity. The two inequivalent surface lattice oxygens are labeled O^A and O^B: O^A is coordinated to three subsurface Co^{3+} atoms (in light blue); O^B is coordinated to two subsurface Co^{3+} atoms and one surface Co^{2+} atom (dark blue).

Both O^A and O^B vacancies lead to minimal surface rearrangement, with the O^A vacancy leading to the least change in surface bond lengths and the O^B vacancy leading to a shortening of the remaining two Co–O^B bonds from 1.788 to 1.769 Å. These results show that the $Co_3O_4(111)$ surface can readily generate and refill oxygen vacancies without loss of surface structure, suggesting robustness and stability consistent with experimental and theoretical findings,[26,28,50] and making it a good candidate as the model for the catalytic surface.

The less negative Bader charge of O^A than that of O^B indicates the increased ability of the O^A oxygen to further gain electrons, so O^A is more electrophilic than O^B and thus is the more favored active site for the homolytic fission of the C–H bond in the ethane ODH reaction. The more negative Bader charge of O^B suggests that it is more nucleophilic in character and more suitable for the heterolytic fission of the C–H bond as part of the metal–oxygen redox pair, where the metal cation Co^{2+} participates as the electrophile. Both the homolytic and heterolytic C–H cleavages will be examined next.

3.2 First C–H activation of ethane

In alkane oxidation reactions over metal oxides, both the full oxidation and ODH reactions proceed first *via* C–H activation onto the surface. Thus, we first studied the activation of the ethane C–H bond by either a surface oxygen or cobalt. It can be characterized as either a homolytic or heterolytic mechanism, *via* the lattice oxygen or lattice cobalt, respectively.[21,51–53] In the homolytic case, the oxygen atom abstracts a hydrogen from the alkane, forming an alkyl radical which then reacts with a nearby lattice oxygen. In the heterolytic case, the reaction occurs over the Co–O acid–base site pair with the lattice Co activating the C–H bond *via* σ-bond metathesis, leading to the formation of Co–C_2H_5 and O–H.

We examined both the heterolytic and homolytic pathways on the $Co_3O_4(111)$ surface. Based on the configuration of the surface cobalt and oxygen, there should be five possible final states. Starting with weakly physisorbed C_2H_6 on the surface, we found the minimum energy paths and transition states leading to the five final states. These transition and final states are illustrated in Fig. 2, while the energy profiles are shown in Fig. 3. For the heterolytic activation (reactions 1A and B), the transition states were found to form a Co–C_2H_5–H–O complex. The barrier for the pathway *via* O^B is 1.02 eV, lower than that *via* O^A (1.11 eV), likely due to the fact that O^A is slightly farther from Co than O^B, which results in a less stable transition state complex. For the homolytic activation (reactions 1C–E), the transition states show the formation of a CH_3CH_2–H–O complex where the C–H–O angle is almost

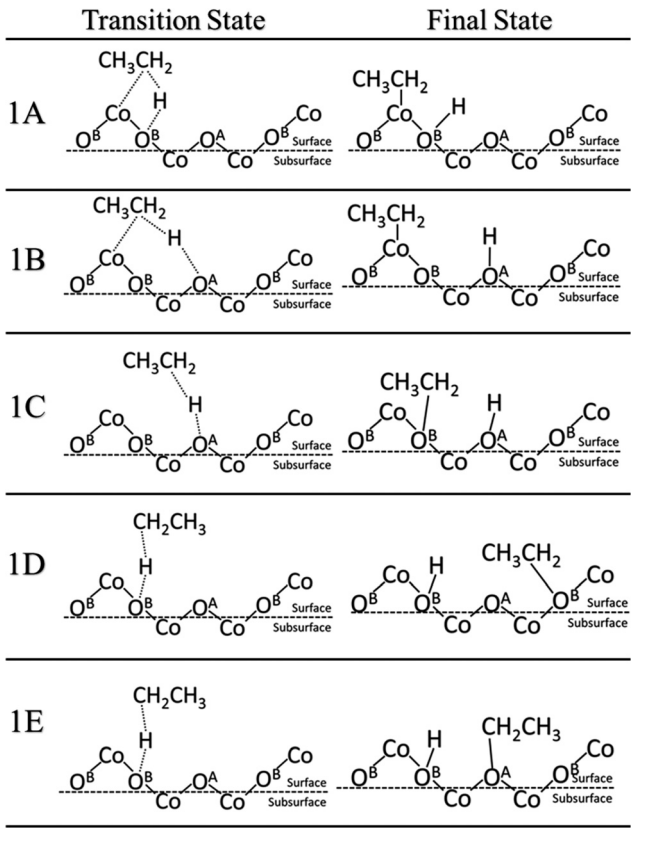

Fig. 2 Transition and final states for the first C–H activation on $Co_3O_4(111)$. Reactions 1A and 1B are Co^{2+}-activated heterolytic reactions. Reactions 1C–E are O-activated homolytic reactions.

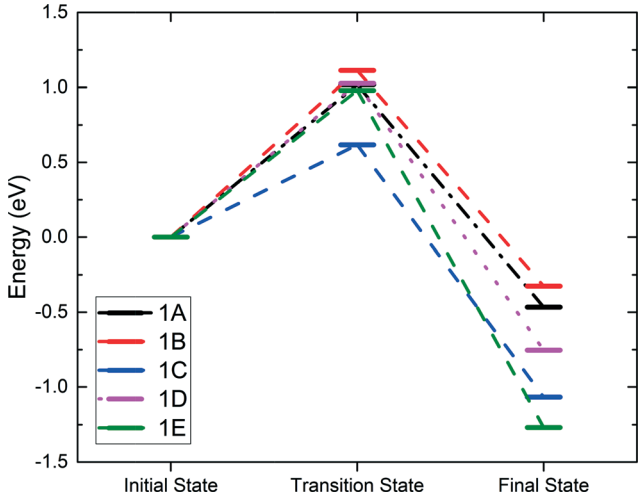

Fig. 3 Energy profiles of the first C–H activation. Reactions 1A and 1B are Co-activated, whereas reactions 1C–1E are O-activated.

180 degrees, while in the final states, the ethyl group attaches to another nearby lattice O. Reaction 1C is activated by the O^A oxygen with a barrier of 0.62 eV, whereas reactions 1D and 1E are both activated by the O^B oxygen with a similar barrier of 0.98 to 1.03 eV. The stronger oxidizing power of O^A than that of O^B, as indicated by the charge analysis, corroborates the lower activation energy of the first C–H activation on O^A.

The energy barriers (E_a) and reaction energies (ΔE) of both the heterolytic and homolytic pathways of 1A–E are compared in Table 1, together with those of propane from another study.[21] We find that our calculated barriers are in very good agreement with the propane barriers for the same surface. It is apparent that the homolytic pathway is both the thermodynamically and kinetically favored reaction path due to the overall lower barriers as well as the more negative reaction energies. The O^A-catalyzed pathway has the lowest barrier by far with a value of 0.62 eV. These results are also in good agreement with the propane DFT results and consistent with the higher bond dissociation energy of the ethane C–H bond.

3.3 Second C–H activation and C_2H_4 formation

We further examined the second C–H activation of ethane following the first C–H activation. Reactions 1A and 1C were selected as the best starting points for the second activation for the heterolytic and homolytic cases, respectively. The subsequent second C–H pathways (transition states and final states) are illustrated in Fig. 4, while the energy profiles are shown in Fig. 5. In the heterolytic case (following 1A), the second C–H bond is activated *via* O^B on the CH_3 group, or β-hydrogen elimination (2A), *via* O^B on the CH_2 group, or α-hydrogen elimination (2B), or *via* O^A by β-hydrogen elimination (2C). We find that the 2C path has the lowest barrier of only 0.39 eV (Fig. 5). In the homolytic case (following 1C), the second C–H bond is activated *via* either O^A by β-hydrogen elimination (2D), O^B by α-hydrogen elimination (2E), or O^A–H in the previous step by α-hydrogen elimination (2F). We found that the 2D and 2E pathways yield very similar barriers of 1.26 eV (Fig. 5). The 2F pathway has a much higher barrier of 2.46 eV, because the presence of a pre-existing adsorbed hydrogen on the lattice O severely deactivates it from further C–H activation.

The barriers and reaction energies of the second C–H activation are compared in Table 2. Most notably, the second C–H activation following the heterolytic pathway (1A then 2C) appears to have lower barriers than that following the homolytic pathway (1C then 2D or 2E). This result is also consistent with the DFT study of propane on the Co_3O_4(110) surface.[21] Reactions 2A, 2C, and 2D *via* β-hydrogen elimination all lead to ethylene formation. In the case of 2A and 2C, we found that desorption of C_2H_4 is uphill by about 1.0 eV, while in the case of 2D, C_2H_4 was found to spontaneously go to the gas phase. Reactions 2B, 2E, and 2F *via* α-hydrogen elimination generate CH_3CH which were found to bind very strongly to the surface Co or O with a strength greater than 2 eV. We expect that the CH_3CH intermediate is unlikely to result in ethylene production and more likely to be part of the further oxidation pathways.

3.4 Hydroxyl clustering, water formation, and water desorption

Following the second C–H activation, ethylene will desorb in the ODH reaction, leaving two lattice O sites with adsorbed hydrogen, that is, the formation of hydroxyls. Previous experimental isotopic studies have thoroughly shown that the oxidation and ODH reactions result in the formation of water containing lattice oxygen.[20] Therefore, these surface hydroxyls will come closer (clustering), then form water, and desorb from the surface, in order for the catalytic cycle to proceed. The simplistic path for hydroxyl clustering is *via* diffusion of the hydrogen atom from a surface hydroxyl to a neighboring lattice oxygen. With two hydroxyl groups nearby, one hydrogen of a hydroxyl can combine with the neighboring hydroxyl to form water. The barrier for a representative H

Table 1 Activation energy E_a and energy of reaction ΔE of the first C–H activation of ethane. Propane E_a and ΔE in a similar study on the same Co_3O_4(111) surface are listed for comparison

No.	Reaction pathway	Ethane E_a (eV)	Ethane ΔE (eV)	Propane E_a (eV) (ref. 21)	Propane ΔE (eV) (ref. 21)
1A	$C_2H_6(g) \rightarrow C_2H_5$–$Co^{2+}$ + O^B–H	1.02	−0.47	0.95	−0.71
1B	$C_2H_6(g) \rightarrow C_2H_5$–$Co^{2+}$ + O^A–H	1.11	−0.33	N/A	N/A
1C	$C_2H_6(g) \rightarrow C_2H_5$–$O^B$ + O^A–H	0.62	−1.07	0.41	−1.41
1D	$C_2H_6(g) \rightarrow C_2H_5$–$O^B$ + O^B–H	1.03	−0.75	0.60	−0.80
1E	$C_2H_6(g) \rightarrow C_2H_5$–$O^A$ + O^B–H	0.98	−1.27	N/A	N/A

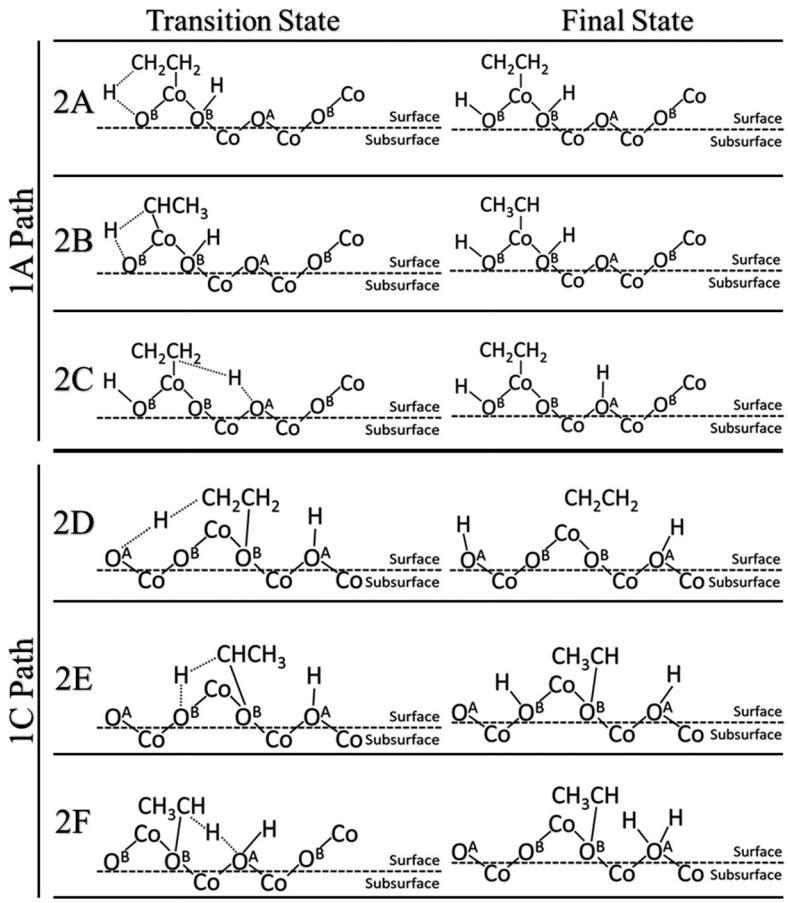

Fig. 4 Transition and final states for the second C–H activation of ethane. Reactions 2A–2C continue from the previous heterolytic reaction 1A. Reactions 2D–2F continue from the previous homolytic reaction 1C.

diffusion from O^A to O^B on the $Co_3O_4(111)$ surface was found to be 1.35 eV (Fig. 6A). Next, we examined the water formation from two neighboring hydroxyl groups (Fig. 6B) and the barrier increases to 2.02 eV.

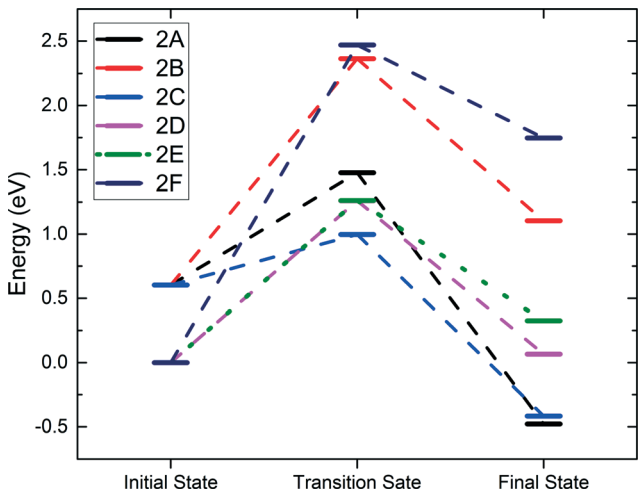

Fig. 5 Energy profiles of the second C–H activation. Reactions 2A–2C follow the 1A path. Reactions 2D–2F follow the 1C path.

After the H–O–H species is formed on the surface (Fig. 6B), it can then desorb to the gas phase. The desorption energy was found to be 0.581 eV, much lower than the lattice-oxygen vacancy formation energy (2.488 eV for the O^A atom). Indeed, the addition of two hydrogen atoms on the same lattice oxygen destabilizes the system and lengthens the Co–O bonds. Oxygen vacancies are then formed following the desorption of water.

3.5 Regeneration of lattice oxygen sites

The oxygen vacancies left from water desorption can react with gas phase O_2 to regenerate the lattice oxygen sites. A

Table 2 Activation energy (E_a) and reaction energy (ΔE) of the second C–H activation of ethane, starting from the most favored Co-activated path (1A) for 2A–2C and O-activated path (1C) for 2D–2F from the first C–H activation

No.	Reaction pathway	E_a (eV)	ΔE (eV)
2A	C_2H_5–Co^{2+} + O^B–H → CH_2CH_2–Co^{2+} + 2O^B–H	0.87	−1.08
2B	C_2H_5–Co^{2+} + O^B–H → CH_3CH–Co^{2+} + 2O^B–H	1.76	0.50
2C	C_2H_5–Co^{2+} + O^B–H → CH_2CH_2–Co^{2+} + O^A–H + O^B–H	0.39	−1.02
2D	C_2H_5–O^B + O^A–H → CH_2CH_2–O^B + 2O^A–H	1.26	0.07
2E	C_2H_5–O^B + O^A–H → CH_3CH–O^B + O^A–H + O^B–H	1.26	0.33
2F	C_2H_5–O^B + O^A–H → CH_3CH–O^B + H–O^A–H	2.47	2.34

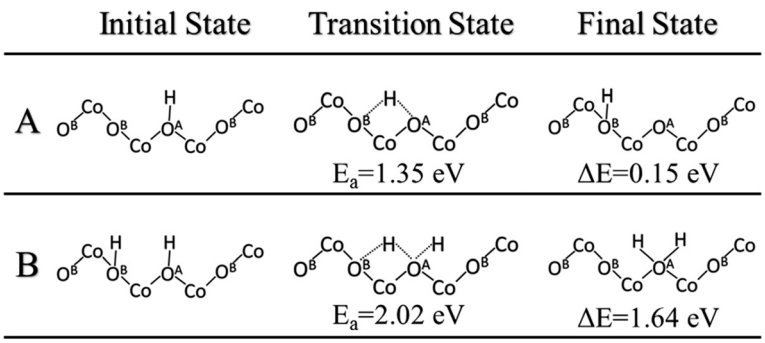

Fig. 6 Initial, transition and final states for hydrogen diffusion across the $Co_3O_4(111)$ surface: A, diffusion of hydrogen from O^A to O^B; B, diffusion of hydrogen from O^B to an O^A–H hydroxyl group.

very likely scenario would be that one gaseous O_2 molecule refills at a double oxygen vacancy site. We found that O_2 first binds vertically on one of the vacancies and then one oxygen atom of O_2 then dissociates to the neighboring vacancy site. We calculated the barrier of this process and found that it occurs *via* a barrier of only 0.51 eV and a reaction energy of −4.24 eV (Fig. 7A). These double vacancies may be generated through the process of continuous water formation/desorption reactions on the surface during the catalytic cycle, or through vacancy diffusion across the surface. The diffusion of these oxygen vacancies was also studied and found to have a barrier of 1.63 eV for a diffusion from a vacancy at O^B to O^A (Fig. 7B). This double-vacancy regeneration model (Fig. 7A) with very low barriers is also consistent with previous theoretical works on the $Co_3O_4(110)$ surface.[19,21] Thus, we can conclude that regeneration of the lattice oxygen sites is highly facile in oxygen-rich environments and unlikely to be a rate-determining step in the overall catalytic cycle.

3.6 Overall energy profile

Fig. 8 shows the overall energy profile including the first and second C–H activations, hydroxyl clustering *via* hydrogen diffusion, and water formation and desorption. We select the 1C–2D homolytic path as the most representative ODH pathway through consideration of both activation energies and reaction energies, and product desorption. We omit the vacancy regeneration portion of the cycle for simplicity as well as the fact that its barriers are quite low in comparison. Fig. 8 shows that the water formation step is the least energetically favored step and a possible rate-determining step in the overall catalytic cycle. Alternative to the 1C–2D path, we also considered a competitive path *via* the 1A–2C heterolytic path where the first C–H activation is *via* Co^{2+} and the second C–H activation is *via* O^A. We found that again water formation is the rate-determining step (RDS) in this mechanism.

A schematic drawing of the complete catalytic cycle for the homolytic path is shown in Fig. 9, composed of the first and second C–H activations, hydrogen diffusion, water formation, and lattice-oxygen regeneration. It starts with C_2H_6 adsorption, followed by the first C–H cleavage on lattice O^A. Then, the second C–H cleavage takes place on another lattice O^A, leading to the formation and desorption of C_2H_4. Next, hydroxyl clusters *via* hydrogen diffusion and water forms from nearby hydroxyl groups. Water desorbs and leaves lattice-oxygen vacancies, which are refilled by molecular oxygen. The cycle repeats.

3.7 Implications of the present DFT results

Our present DFT study of ethane ODH on the $Co_3O_4(111)$ surface presents several interesting perspectives regarding the reaction characteristics. First, we find that for ethane, the first step of the reaction occurs *via* the activation of its C–H bond over either the Co^{2+} or the O^A/O^B atoms. While the first C–H activation is strongly favored towards the O-activated homolytic pathway, the second C–H activation is in fact more favored towards the heterolytic pathway. In reality, it is likely

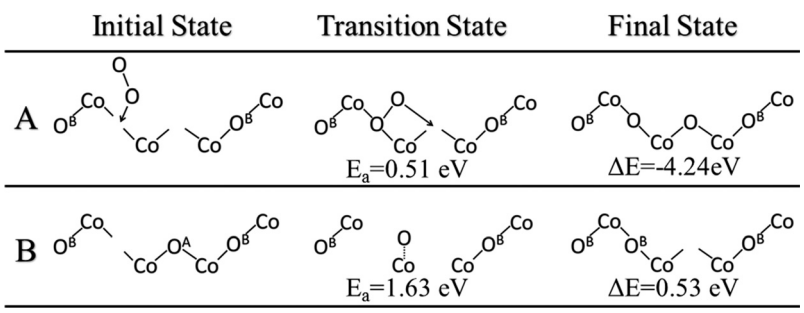

Fig. 7 (A) Regeneration of lattice oxygen on $Co_3O_4(111)$ *via* reaction of double oxygen vacancies with gaseous molecular oxygen. (B) Vacancy diffusion on the $Co_3O_4(111)$ surface from the O^B site to the O^A site.

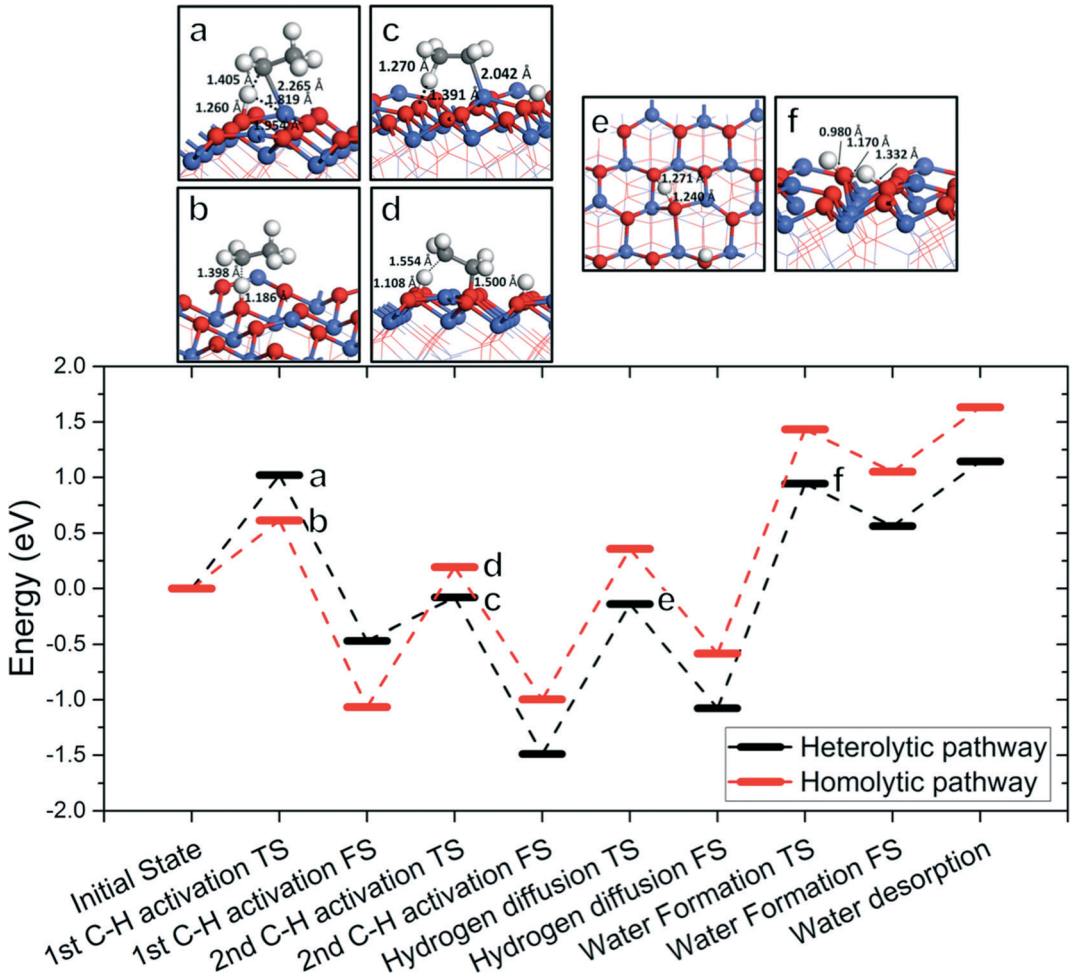

Fig. 8 Lower panel: The overall energy profile of ODH of ethane to ethylene on $Co_3O_4(111)$; upper panel: structures (with key distances) corresponding to the transition states a–f in the energy profile (Co, blue; O, red; C, gray; H, white). In the energy profile, the C–H cleavages follow the 1C–2D homolytic path (red) or the 1A–2C heterolytic path (black) with energetics from Fig. 2–5, while the hydrogen diffusion and water formation energies are from Fig. 6.

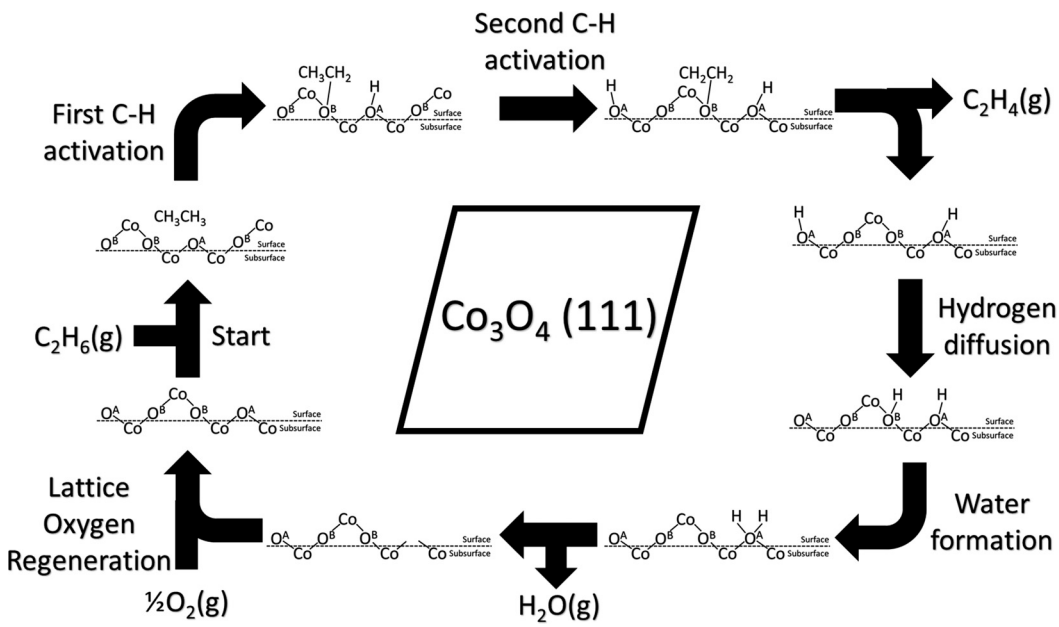

Fig. 9 Schematic drawing of the complete catalytic cycle of ethane ODH on the $Co_3O_4(111)$ surface.

for both pathways to participate in the formation of ethylene; however, without further kinetic analysis, it would be very difficult to quantify their respective contributions towards forming the ODH product.

Next, we have found the vacancy formation energy and Bader charge of the lattice oxygen to be good descriptors of the catalytic activity of the lattice oxygen. We were able to predict the O^A oxygen to have lower barriers for C–H activation than the O^B oxygen. We would expect this trend to hold for lattice oxygen atoms of different Co_3O_4 surfaces, such as (110), (100), and (112). These surfaces could be important for Co_3O_4 nanocatalysts with different morphologies.

We find that the water formation step of the catalytic cycle on the pure (111) surface appears to be the RDS, while experiments show that changing the alkane will change the overall barriers,[54] thus suggesting that the C–H activation barrier is significant to the overall rates. Based on preliminary DFT results, we believe that the hydroxylation of the surface will affect the energy profile by increasing the barriers of C–H activation and reducing the barriers of H_2O formation. In this model, we can then expect that the actual experimental energy profile will have the C–H activation and water formation barriers approach in energy at a steady-state hydrogen coverage of the surface. Thus, varying C–H bond strength would in fact affect the rates of the overall ODH reaction.

Experimental findings have indeed shown that surface hydroxylation occurs on the surfaces of metal oxides as the dominant species during and after a reaction.[55,56] In addition, water formation and consequently water concentration were found to affect the rates of the ODH/oxidation reactions on many studied metal oxides.[55,57–59] This phenomenon occurs for CO and CH_4 oxidation on Co_3O_4 as well.[56,60,61] These experimental findings support our conclusion that water formation is an important step of ethane ODH on Co_3O_4(111). This phenomenon is notably absent in CO oxidation, which is consistent with experimental observations of CO oxidations having much lower barriers and reaction temperatures than alkane oxidation. The coverage effect of surface hydroxyl groups on the catalytic pathways thus warrants further studies.

The experimental work on ethane ODH on Co_3O_4 nanorods[38] has focused on ethylene/CO_2 selectivity and ethylene yield as a function of surface modification by Si and Ge oxides. Detailed kinetic data such as reaction rates and apparent activation energy on the unmodified Co_3O_4 nanorods are still not available for a direct comparison. To compare with the experimental ethylene/CO_2 selectivity, the complete pathway of ethane combustion has to be mapped out, which requires substantial and deeper investigation and is beyond the scope of the present work. A joint experimental and computational study is expected in the near future to directly compare the computational results and the experimental data.

The present DFT study focuses on the (111) surface based on the STEM images of our Co_3O_4 nanorod sample (Fig. 1), but other facets may also exist such as the (100) and (110) surfaces depending upon the preparation methods and calcination temperature. The different facets can affect the energetics of the elementary steps because the oxygen reactivity can be different. For example, the (110)-B surface of Co_3O_4 has a twofold-coordinate oxygen site, in contrast with the threefold-coordinate oxygen sites on the (111) surface. How this twofold-coordinate oxygen site on the (110)-B surface would change the energetics of ethane ODH steps is a question that we intend to find out in a future study.

4. Conclusions

We have studied the oxidative dehydrogenation (ODH) of ethane to ethylene on the Co_3O_4(111) surface with DFT+U, in order to understand the mechanism on Co_3O_4 nanorods. The more reactive lattice oxygen (O^A) was found to yield the lowest barriers for the first C–H activation, consistent with our predictions based on vacancy formation energy and Bader charges. Overall, we found the barriers for the first C–H activation to be lower for the homolytic pathway (~0.62 eV), but the barriers for the second C–H activation to be lower for the heterolytic pathway. The cleaved hydrogen from C_2H_6 forms hydroxyl groups on Co_3O_4(111), which can cluster *via* hydrogen diffusion. Water formation from nearby hydroxyl groups and desorption to leave oxygen vacancies on the surface were found to have a large activation energy (2.02 eV) and are likely to be the rate-determining step. These vacancies can readily react with oxygen molecules in gas phase to regenerate the lattice oxygen sites. These insights will help understand the role of the surface orientation of the Co_3O_4 nanocatalysts in improving the selectivity and yield of alkane-to-alkene conversion through ODH.

Acknowledgements

This work was mainly supported by the Chemical Sciences, Geosciences and Biosciences Division, Office of Basic Energy Sciences, Office of Science, U.S. Department of Energy under Grant No. DE-SC0014561. This research used resources of the National Energy Research Scientific Computing Center, a DOE Office of Science User Facility supported by the Office of Science of the U.S. Department of Energy.

References

1 F. Cavani, N. Ballarini and A. Cericola, *Catal. Today*, 2007, **127**, 113–131.
2 A. H. Tullo, *Chem. Eng. News*, 2001, **79**, 18.
3 E. Heracleous, M. Machli, A. A. Lemonidou and I. A. Vasalos, *J. Mol. Catal. A: Chem.*, 2005, **232**, 29–39.
4 G.-L. Dai, Z.-P. Liu, W.-N. Wang, J. Lu and K.-N. Fan, *J. Phys. Chem. C*, 2008, **112**, 3719–3725.
5 H. Fu, Z.-P. Liu, Z.-H. Li, W.-N. Wang and K.-N. Fan, *J. Am. Chem. Soc.*, 2006, **128**, 11114–11123.
6 M. Lezanska, G. S. Szymanski, P. Pietrzyk, Z. Sojka and J. A. Lercher, *J. Phys. Chem. C*, 2007, **111**, 1830–1839.
7 E. Thorsteinson, T. Wilson, F. Young and P. Kasai, *J. Catal.*, 1978, **52**, 116–132.

8 P. Botella, E. Garcıa-González, A. Dejoz, J. L. Nieto, M. Vázquez and J. González-Calbet, *J. Catal.*, 2004, **225**, 428–438.
9 K. Chen, A. T. Bell and E. Iglesia, *J. Catal.*, 2002, **209**, 35–42.
10 E. Heracleous and A. Lemonidou, *J. Catal.*, 2010, **270**, 67–75.
11 X. Sun, B. Li and H. Metiu, *J. Phys. Chem. C*, 2013, **117**, 23597–23608.
12 C. A. Gartner, A. C. van Veen and J. A. Lercher, *ChemCatChem*, 2013, **5**, 3196–3217.
13 A. Qiao, V. N. Kalevaru, J. Radnik, A. Duvel, P. Heitjans, A. S. H. Kumar, P. S. S. Prasad, N. Lingaiah and A. Martin, *Ind. Eng. Chem. Res.*, 2014, **53**, 18711–18721.
14 C. A. Gartner, A. C. van Veen and J. A. Lercher, *J. Am. Chem. Soc.*, 2014, **136**, 12691–12701.
15 H. H. Kristoffersen and H. Metiu, *J. Phys. Chem. C*, 2015, **119**, 8681–8691.
16 H. B. Zhu, D. C. Rosenfeld, D. H. Anjum, S. S. Sangaru, Y. Saih, S. Ould-Chikh and J. M. Basset, *J. Catal.*, 2015, **329**, 291–306.
17 X. Chen, Q. L. Yang, B. Z. Chu, H. An and Y. Cheng, *RSC Adv.*, 2015, **5**, 91295–91301.
18 L. Smolakova, M. Kout, E. Koudelkova and L. Capek, *Ind. Eng. Chem. Res.*, 2015, **54**, 12730–12740.
19 D. E. Jiang and S. Dai, *Phys. Chem. Chem. Phys.*, 2011, **13**, 978–984.
20 F. F. Tao, J. J. Shan, L. Nguyen, Z. Wang, S. Zhang, L. Zhang, Z. Wu, W. Huang, S. Zeng and P. Hu, *Nat. Commun.*, 2015, **6**, 7798.
21 E. C. Tyo, C. Yin, M. Di Vece, Q. Qian, G. Kwon, S. Lee, B. Lee, J. E. DeBartolo, S. Seifert, R. E. Winans, R. Si, B. Ricks, S. Goergen, M. Rutter, B. Zugic, M. Flytzani-Stephanopoulos, Z. W. Wang, R. E. Palmer, M. Neurock and S. Vajda, *ACS Catal.*, 2012, **2**, 2409–2423.
22 S. Zhang, J.-J. Shan, Y. Zhu, A. I. Frenkel, A. Patlolla, W. Huang, S. J. Yoon, L. Wang, H. Yoshida, S. Takeda and F. Tao, *J. Am. Chem. Soc.*, 2013, **135**, 8283–8293.
23 X. W. Xie, Y. Li, Z. Q. Liu, M. Haruta and W. J. Shen, *Nature*, 2009, **458**, 746–749.
24 X. Liu, G. Qiu and X. Li, *Nanotechnology*, 2005, **16**, 3035.
25 F. Zasada, J. Gryboś, P. Indyka, W. Piskorz, J. Kaczmarczyk and Z. Sojka, *J. Phys. Chem. C*, 2014, **118**, 19085–19097.
26 W. Meyer, K. Biedermann, M. Gubo, L. Hammer and K. Heinz, *J. Phys.: Condens. Matter*, 2008, **20**, 265011.
27 J. Chen and A. Selloni, *Phys. Rev. B: Condens. Matter Mater. Phys.*, 2012, **85**, 085306.
28 X.-L. Xu, Z.-H. Chen, Y. Li, W.-K. Chen and J.-Q. Li, *Surf. Sci.*, 2009, **603**, 653–658.
29 P. Ferstl, S. Mehl, M. A. Arman, M. Schuler, A. Toghan, B. Laszlo, Y. Lykhach, O. Brummel, E. Lundgren, J. Knudsen, L. Hammer, M. A. Schneider and J. Libuda, *J. Phys. Chem. C*, 2015, **119**, 16688–16699.
30 Y. Li, B. Tan and Y. Wu, *J. Am. Chem. Soc.*, 2006, **128**, 14258–14259.
31 F. Zasada, W. Piskorz, J. Janas, J. Gryboś, P. Indyka and Z. Sojka, *ACS Catal.*, 2015, **5**, 6879–6892.
32 K. Biedermann, M. Gubo, L. Hammer and K. Heinz, *J. Phys.: Condens. Matter*, 2009, **21**, 185003.
33 C. Doornkamp and V. Ponec, *J. Mol. Catal. A: Chem.*, 2000, **162**, 19–32.
34 P. Broqvist, *J. Catal.*, 2002, **210**, 198–206.
35 X. Y. Pang, C. Liu, D. C. Li, C. Q. Lv and G. C. Wang, *ChemPhysChem*, 2013, **14**, 204–212.
36 X.-L. Xu, E. Yang, J.-Q. Li, Y. Li and W.-K. Chen, *ChemCatChem*, 2009, **1**, 384–392.
37 R. Pestman, R. Koster, J. Pieterse and V. Ponec, *J. Catal.*, 1997, **168**, 255–264.
38 J. Liu, S. Zhang, Y. Zhou, V. Fung, L. Nguyen, D. E. Jiang, W. Shen, J. Fan and F. F. Tao, *ACS Catal.*, DOI: 10.1021/acscatal.5b02900.
39 X. W. Xie, P. J. Shang, Z. Q. Liu, Y. G. Lv, Y. Li and W. J. Shen, *J. Phys. Chem. C*, 2010, **114**, 2116–2123.
40 G. Kresse and J. Furthmuller, *Comput. Mater. Sci.*, 1996, **6**, 15–50.
41 G. Kresse and J. Furthmuller, *Phys. Rev. B: Condens. Matter Mater. Phys.*, 1996, **54**, 11169–11186.
42 S. Dudarev, G. Botton, S. Savrasov, C. Humphreys and A. Sutton, *Phys. Rev. B*, 1998, **57**, 1505.
43 J. P. Perdew, K. Burke and M. Ernzerhof, *Phys. Rev. Lett.*, 1996, **77**, 3865.
44 G. Kresse and D. Joubert, *Phys. Rev. B: Condens. Matter Mater. Phys.*, 1999, **59**, 1758.
45 P. E. Blöchl, *Phys. Rev. B: Condens. Matter Mater. Phys.*, 1994, **50**, 17953–17979.
46 H. J. Monkhorst and J. D. Pack, *Phys. Rev. B: Solid State*, 1976, **13**, 5188.
47 P. Dutta, M. S. Seehra, S. Thota and J. Kumar, *J. Phys.: Condens. Matter*, 2008, **20**, 015218.
48 G. Henkelman and H. Jónsson, *J. Chem. Phys.*, 1999, **111**, 7010.
49 http://theory.cm.utexas.edu/vtsttools/.
50 L. Hu, Q. Peng and Y. Li, *J. Am. Chem. Soc.*, 2008, **130**, 16136–16137.
51 G. Martin and C. Mirodatos, *Fuel Process. Technol.*, 1995, **42**, 179–215.
52 G. Fu, X. Xu, X. Lu and H. Wan, *J. Am. Chem. Soc.*, 2005, **127**, 3989–3996.
53 M. C. Holthausen and W. Koch, *J. Am. Chem. Soc.*, 1996, **118**, 9932–9940.
54 Z. Tian, N. Bahlawane, F. Qi and K. Kohse-Höinghaus, *Catal. Commun.*, 2009, **11**, 118–122.
55 M. D. Argyle, K. Chen, A. T. Bell and E. Iglesia, *J. Phys. Chem. B*, 2002, **106**, 5421–5427.
56 G. B. Hoflund and Z. Li, *Appl. Surf. Sci.*, 2006, **253**, 2830–2834.
57 M. D. Argyle, K. Chen, A. T. Bell and E. Iglesia, *J. Catal.*, 2002, **208**, 139–149.
58 K. Chen, A. T. Bell and E. Iglesia, *J. Phys. Chem. B*, 2000, **104**, 1292–1299.
59 B. Kilos, A. T. Bell and E. Iglesia, *J. Phys. Chem. C*, 2009, **113**, 2830–2836.
60 Y. Yu, T. Takei, H. Ohashi, H. He, X. Zhang and M. Haruta, *J. Catal.*, 2009, **267**, 121–128.
61 F. Grillo, M. M. Natile and A. Glisenti, *Appl. Catal., B*, 2004, **48**, 267–274.